Inferring the Mean Thickness of the Outer Ice Shell of Enceladus from Diurnal Crustal Deformation

Alexander Berne[1], Mark Simons[1], James Tuttle Keane[2], Ryan S. Park[2]

[1]California Institute of Technology, Pasadena, CA 91125 USA

[2]Jet Propulsion Laboratory, California Institute of Technology, Pasadena, CA 91109 USA

Key Points:

- We show faults, crustal weak zones, and thickness variations in the ice shell measurably impact tidal deformation at Enceladus.
- We find that structural heterogeneities could bias inferences of ice shell thickness using diurnal Love numbers by up to 41%.
- Heterogeneities near the South Pole could drive differences of up to 35% between Love number values at different spherical harmonic orders.

Corresponding author: Alexander Berne, aberne@caltech.edu

Abstract

The thickness of the outer ice shell plays an important role in several geodynamical processes at ocean worlds. Here, we show that observations of tidally-driven diurnal surface displacements can constrain the mean ice shell thickness, $\tilde{d}_{ice}$. Such estimates are sensitive to any significant structural features that break spherical symmetry such as faults and lateral variation in ice shell thickness and structure. We develop a finite-element model of Enceladus to calculate diurnal tidal displacements for a range of $\tilde{d}_{ice}$ values in the presence of such structural heterogeneities. Consistent with results from prior studies, we find that the presence of variations in ice shell thickness can significantly amplify deformation in thinned regions. If major faults are also activated by tidal forcing—such as Tiger Stripes on Enceladus—their characteristic surface displacement patterns could easily be measured using modern geodetic methods. Within the family of Enceladus models explored, estimates of $\tilde{d}_{ice}$ that assume spherical symmetry a priori can deviate from the true value by as much as $\sim 41\%$ when structural heterogeneities are present. Additionally, we show that crustal heterogeneites near the South Pole produce differences of up to 35% between Love numbers evaluated at different spherical harmonic orders. A $\sim 41\%$ range in estimates of $\tilde{d}_{ice}$ from Love numbers is smaller than that found with approaches relying on static gravity and topography ($\sim 250\%$) or analyzing diurnal libration amplitudes ($\sim 85\%$) to infer $\tilde{d}_{ice}$ at Enceladus. As such, we find that analysis of diurnal tidal deformation is a relatively robust approach to inferring mean crustal thickness.

Plain Language Summary

For ocean worlds such as Enceladus, it is useful to determine the thicknesses of the outer ice crust—as it provides information about the depth of the ocean, the thermal evolution of the body, and the rate at which material at the surface can be recycled to the ocean by burial processes. By measuring the deformation of the surface in response to tidal forces, we can infer the mean ice shell thickness at Enceladus. Here, we show that the presence of large fault systems (such as the Tiger Stripes) or variations in the thickness of the ice shell (i.e., structural heterogeneities) affects Enceladus's response to tides. We find that estimates of ice shell thickness that ignore the potential impact of structural heterogeneities can deviate from true thickness values by up to 41%. This deviation is smaller than that found with other approaches that rely on analyzing gravity and

topography ($\sim 250\%$) or the periodic rigid rotation of the ice shell ($\sim 85\%$) to infer Enceladus's mean ice shell thickness. As such, despite the presence of heterogeneities, measurements of tidal deformation at Enceladus would be a powerful probe of subsurface structure.

1 Introduction

Enceladus, a moon orbiting Saturn approximately every 32.9 hrs, is demonstratively geologically active (Porco et al., 2006; Spencer et al., 2006; Hansen et al., 2006; Ingersoll et al., 2020). Erupting jets at the body's surface align with the position of four prominent, evenly spaced surface fractures (informally known as 'Tiger Stripes') (Porco et al., 2006). These fractures produce jets or geysers that are the source of a water-ice-dominated plume emanating from the South Polar Terrain (SPT). The Tiger Stripes correlate with the position of anomalously high heat flux and regional thinning at the SPT (Spencer et al., 2006; Porco et al., 2014). Moreover, jet activity varies with orbital phase to produce maxima in plume brightness near orbital apoapse and periapse (Ingersoll et al., 2020). The correlation of the plume brightness oscillation period and Enceladus's orbital period strongly suggests that diurnal tides regulate heat and mass transport in the outer ice shell (Hurford et al., 2007). We explore the interactions between crustal structure and diurnal deformation to improve our understanding of the interior dynamics of Enceladus.

Constraints on ice shell structure, in particular outer shell mean thickness $\tilde{d}_{ice}$, provide a first-order constraint on the thermal properties, interior structure, and potential for habitability of any ocean world. $\tilde{d}_{ice}$ is an essential parameter for understanding the total heat budget (Roberts & Nimmo, 2008), the potential for convection within the ice shell (Mitri & Showman, 2005), the radial extent of the core and ocean (Hemingway & Mittal, 2019), and the rate at which oxidized material cycles between the surface and the ocean through burial processes (Zolotov & Shock, 2004). $\tilde{d}_{ice}$ also constrains plausible tidal heating mechanisms on Enceladus including viscous dissipation in the crust (Souček et al., 2019) and turbulent ocean flow (Hay & Matsuyama, 2019; Tyler, 2020).

Several approaches currently exist to infer $\tilde{d}_{ice}$. Static gravity and topography admittance modelling (Iess et al., 2014; McKinnon, 2015; Hemingway & Mittal, 2019; Akiba et al., 2022) and diurnal shell libration amplitude measurements (Thomas et al., 2016; Van Hoolst et al., 2016) yield estimates of $\tilde{d}_{ice}$ for Enceladus between 17–60 km ($\sim 250\%$)

and 14–26 km ($\sim 85\%$), respectively. These methods rely on the presence of large-scale non-hydrostatic surface topography and a hydrostatic core, or alternatively, a short orbital period (i.e., that is comparable to the resonant frequency of the ice shell of a few days). Here, we explore an alternative approach that relies on the analysis of the response to short-period (i.e., diurnal) tidal forcing. Inferences of $\tilde{d}_{ice}$ from analysis of diurnal tides are relatively insensitive to assumptions regarding the core and are not contingent upon fortuitous structural or orbital conditions (e.g., a short orbital period or the presence of non-hydrostatic topography) at Enceladus.

Differential gravitational attraction to a central, parent body (e.g., a planet) produces tides on orbiting satellites. Over timescales substantially greater than that of the orbital period (i.e., long-period), satellites deform as viscous fluids and the ultimate response to tidal forces is sensitive to radially varying internal density structure (e.g., Hubbard & Anderson, 1978). Bodies with eccentric orbits around their parent bodies experience an additional tidal force (i.e., the eccentricity or diurnal tide) which operates at a period equal to that of the orbit. At this timescale, any non-fluid interior layers may deform viscoelastically. For ocean-world bodies (i.e., where the outer ice shell and silicate core are mechanically decoupled by an intervening liquid ocean) deformation of the outer shell in response to diurnal tides is then relatively insensitive to the deep internal structure but is highly sensitive to $\tilde{d}_{ice}$. Measurement of time-varying gravity or surface displacement can therefore be used to directly infer $\tilde{d}_{ice}$.

The radial response of a body to time-dependent forcing can be described using gravitational and shape Love numbers (k_l and h_l respectively) that depend on spherical harmonic degree l (Love, 1909). The $l = 2$ diurnal Love numbers k_2^d and h_2^d track the very long-wavelength elastic response of bodies to diurnal tides and are sensitive to long-wavelength elastic structure (i.e., $\tilde{d}_{ice}$). We will demonstrate that there only exists a unique relationship between a body's response and a load at $l = 2$ for the limiting case of a fully spherically symmetric body. More generally, inferences of $\tilde{d}_{ice}$ from diurnal Love numbers at Enceladus requires accounting for the potential impact of non-spherically symmetric structure.

For an arbitrary 3D structure, we can formulate a general linear relationship between spherical harmonics V_{lm} (i.e., of degree l and order m) of a driving gravitational

potential $V(\bar{\Omega})$ which deforms (i.e., drives mass movement) within a body and generates harmonics $U_{l'm'}$ of an induced gravitational potential potential $U(\bar{\Omega})$:

$$V(\bar{\Omega}) = \sum_{l=0}^{\infty} \sum_{m=-l}^{l} V_{lm} Y_{lm}(\bar{\Omega}) \tag{1a}$$

$$U(\bar{\Omega}) = \sum_{l'=0}^{\infty} \sum_{m'=-l'}^{l'} U_{l'm'} Y_{l'm'}(\bar{\Omega}) \tag{1b}$$

where $Y_{lm}(\bar{\Omega})$ denote real spherical harmonics, the prime ($'$) denotes induced components, and $\bar{\Omega}$ is the angular position variable comprising a co-latitude and longitude pair (θ, ϕ) in a reference frame whose origin is fixed to Enceladus's center of mass (Note: we restrict our analysis to the induced gravitational response but could easily apply the methodology discussed in this section to derive the induced topographic response). For a linear elastic solid, deformation is linearly related to forcing (see also Supplementary S1.1). The tidal forcing harmonics V_{lm} accordingly map to harmonics $U_{l'm'}$ via linear Green's functions $\gamma_{lm}^{l'm'}$ which describe the elastic structure of a body:

$$\begin{bmatrix} U_{l'm'} \\ \vdots \\ \vdots \\ U_{\infty\infty} \end{bmatrix} = \begin{bmatrix} \gamma_{lm}^{l'm'} & \cdots & \cdots & \gamma_{\infty\infty}^{l'm'} \\ \vdots & \ddots & & \vdots \\ \vdots & & \ddots & \vdots \\ \gamma_{lm}^{\infty\infty} & \cdots & \cdots & \gamma_{\infty\infty}^{\infty\infty} \end{bmatrix} \begin{bmatrix} V_{lm} \\ \vdots \\ \vdots \\ V_{\infty\infty} \end{bmatrix} \tag{2}$$

Equation 2 demonstrates that the response of a body (i.e., defined as $U_{l'm'}/V_{lm}$) will generally vary in time due to the changing shape of an applied load (i.e., time-variable V_{lm} components) *despite* a fixed elastic structure. For diurnal tides, the driving potential is comprised of three harmonics V_{20}, V_{22}, and $V_{2\,\text{-}2}$ (Murray & Dermott, 1999) and Equation 2 simplifies to:

$$\begin{bmatrix} U_{l'm'} \\ \vdots \\ \vdots \\ U_{\infty\infty} \end{bmatrix} = \begin{bmatrix} \gamma_{20}^{l'm'} & \gamma_{22}^{l'm'} & \gamma_{2\,\text{-}2}^{l'm'} \\ \vdots & \vdots & \vdots \\ \vdots & \vdots & \vdots \\ \gamma_{20}^{\infty\infty} & \gamma_{20}^{\infty\infty} & \gamma_{2\,\text{-}2}^{\infty\infty} \end{bmatrix} \begin{bmatrix} V_{20} \\ V_{22} \\ V_{2\,\text{-}2} \end{bmatrix} \tag{3}$$

$U_{lm} \neq 0$ for $l \neq 2$ indicate a coupling between forcing and response across spatial scales (i.e., 'mode coupling'; Dahlen & Tromp, 1998). To derive Love numbers, we restrict our analysis to the U_{20}, U_{22}, and $U_{2\,\text{-}2}$ components of the induced gravitational potential field (Note that $U_{lm} = 0$ for $l = 1$ in a reference frame whose origin is fixed to Enceladus's center of mass). Equation 3 then simplifies to:

$$\begin{bmatrix} U_{20} \\ U_{22} \\ U_{2\,\text{-}2} \end{bmatrix} = \begin{bmatrix} \gamma_{20}^{20} & \gamma_{22}^{20} & \gamma_{2\,\text{-}2}^{20} \\ \gamma_{20}^{22} & \gamma_{22}^{22} & \gamma_{2\,\text{-}2}^{22} \\ \gamma_{20}^{2\,\text{-}2} & \gamma_{22}^{2\,\text{-}2} & \gamma_{2\,\text{-}2}^{2\,\text{-}2} \end{bmatrix} \begin{bmatrix} V_{20} \\ V_{22} \\ V_{2\,\text{-}2} \end{bmatrix} \tag{4}$$

The individual components $\gamma_{lm}^{l'm'}$ in Equation 4 contain information regarding the sphericity of a body's elastic structure. For a non-rigid body, diagonal components (i.e., $\gamma_{20}^{20}, \gamma_{22}^{22}, \gamma_{2\,\text{-}2}^{2\,\text{-}2}$) are always non-zero and are principally sensitive to bulk elastic properties (e.g., $\tilde{d}_{ice}$; Wahr et al., 2006). Off-diagonal components (i.e., γ_{22}^{20}, γ_{20}^{22}, $\gamma_{2\,\text{-}2}^{22}$, $\gamma_{2\,\text{-}2}^{20}$, $\gamma_{22}^{2\,\text{-}2}$, $\gamma_{20}^{2\,\text{-}2}$) represent coupling between forcing and response at mutually distinct harmonics. At spatial wavelengths significantly greater than $\tilde{d}_{ice}$, the outer ice crust of spherically symmetric ocean worlds conform to the shape of driving potential surfaces (i.e., following the thin-plate approximation originally derived from beam theory; Levinson, 1984). According to Equation 4, distinct diagonal components or non-zero off-diagonal components therefore imply the presence of non-spherically symmetric structure. For a spherically symmetric body, $\gamma_{22}^{20} = \gamma_{20}^{22} = \gamma_{2\,\text{-}2}^{22} = \gamma_{2\,\text{-}2}^{20} = \gamma_{22}^{2\,\text{-}2} = \gamma_{20}^{2\,\text{-}2} = 0$ and $\gamma_{20}^{20} = \gamma_{22}^{22} = \gamma_{2\,\text{-}2}^{2\,\text{-}2} = k_2^d$. Equation 4 then simplifies to:

$$\begin{bmatrix} U_{20} \\ U_{22} \\ U_{2\,\text{-}2} \end{bmatrix} = \begin{bmatrix} k_2^d & 0 & 0 \\ 0 & k_2^d & 0 \\ 0 & 0 & k_2^d \end{bmatrix} \begin{bmatrix} V_{20} \\ V_{22} \\ V_{2\,\text{-}2} \end{bmatrix} \tag{5}$$

We can define 'effective' Love numbers k_{2m}^d as quantities which track U_{2m} normalized by V_{2m} (i.e., $k_{2m} = U_{2m}/V_{2m}$). According to Equation 5, a unique relationship between harmonics U_{2m} and V_{2m} exists only for spherically symmetric structures (i.e., $k_{2m}^d \rightarrow k_2^d$). More generally, k_{2m}^d are sensitive to non-spherically symmetric structure and the overall shape of the load (i.e., combination of V_{20}, V_{22}, and $V_{2\,\text{-}2}$) such that $k_{20}^d \neq k_{22}^d \neq k_{2\,\text{-}2}^d$ (i.e., 'order splitting' or 'spectral leakage') (Behounkova et al., 2017; Ermakov et al., 2021; Vance et al., 2021). Several structures are expected to break spherical symmetry at Enceladus including lateral variations in thickness of the ice shell, structurally weak (e.g., highly fractured or damaged) zones, or the presence of major fault structures (Behounkova et al., 2017). We therefore expect that diurnal Love numbers are not directly sensitive to $\tilde{d}_{ice}$ at Enceladus and inferences of $\tilde{d}_{ice}$ from k_{2m}^d (or h_{2m}^d) should account for the potential influence of structural heterogneities in the outer ice crust.

Several studies describe the relationship between elastic structure and diurnal deformation at Enceladus. Wahr et al., (2006) develop analytic expressions to calculate k_{2m}^d

and h^d_{2m} from eccentricity tides at ocean worlds using an approach that only applies to spherically symmetric models. Beuthe (2018) extends this analysis of k^d_{2m} and h^d_{2m} to allow for variations in crustal thickness but assumes a thin-shelled approximation and does not include the potential impact of faults. The most sophisticated models to date by Souček et al., (2016), Behounkova et al., (2017), Souček et al., (2019), and Sládková et al., (2021) simulate deformation using finite-element models (FEM) of the outer ice shell with both variations in ice thickness and weak zones. These studies do not specifically address the relationship between deformation and $\tilde{d}_{ice}$ and exclude effects from a broader range of structural heterogeneities inferred from surface geology at Enceladus including large circum-tectonic boundaries and extensional fractures extending radially outward from the South Polar Terrain (i.e., chasma).

Here, we explore how estimates of $\tilde{d}_{ice}$, based on analysis of diurnal tides, are potentially impacted by structural heterogeneities within the ice crust of Enceladus. We simulate deformation on tidally-loaded quasi-spherical shells using a FEM and compare results from six sets of end member models of Enceladus:

1. A spherically symmetric ice shell.
2. An ice shell with variations in thickness.
3. An ice shell with faults at Tiger Stripe locations.
4. An ice shell with 'weak zones' (regions of reduced shear modulus) at locations corresponding to the position of additional structures inferred from Enceladus's geology (i.e., chasma and circum-tectonic boundaries).
5. An ice shell with both variations in thickness and faults.
6. An ice shell with faults, variations in thickness, and weak zones.

We parameterize the response of the shell by calculating Love numbers k^d_{20}, k^d_{22}, $k^d_{2\text{-}2}$ and h^d_{20}, h^d_{22}, $h^d_{2\text{-}2}$, from deformed geometries and compare these predicted values with those predicted from models without structural heterogeneities. We then explore the challenge of inferring $\tilde{d}_{ice}$ from Love numbers posed by the presence of structural heterogeneities in the crust. We conclude by highlighting the potential for analyzing diurnal tides to determine $\tilde{d}_{ice}$ both for Enceladus as well as for other ocean worlds.

2 Methods

We develop a quasi-spherical FEM of Enceladus that allows for structural heterogeneities in the ice shell and that can be used to predict the elastic response of the body to diurnal tidal loads. We first build an FEM mesh that reflects desired structural heterogeneities. We then use a modified version of the finite-element code PyLith (Aagaard et al., 2007) to calculate displacements on models subjected to tidal forcing. In post-processing, we extract $l = 2$ Love numbers from model displacements. We describe each of these steps in detail below.

2.1 Model Preparation

We consider six types of models that differ in the style of structural heterogeneity assumed: (1) a *Base* model without structural heterogeneities; (2) a model with large scale faults (i.e., *Faulted*); (3) a model with Lateral Thickness Variations (i.e., LTV); (4) a model with weak zones at locations coincident with major geologic structures (i.e., WZ); (5) a combined model with faults and Lateral Thickness Variations (i.e., *Faulted+*LTV); and (6) a combined model with faults, Lateral Thickness Variations, and weak zones (i.e., *Faulted+*LTV*+*WZ). For each model, we develop a mesh with tetrahedral elements using the software package CUBIT (Skroch et al., 2019; CoreForm, 2020) and refine cell size in regions which locally exhibit high strain (e.g., near faults). Minimum and maximum cell sizes (i.e., tetrahedra cell edge lengths) are 1 and 12 km respectively throughout the mesh. For tetrahedra along the faults, we limit maximum cell size to 3 km and achieve a vertical resolutions as fine as 1 - 2 km across each interface. Example snapshots of our mesh geometry are shown in Figure 1. We perform a mesh convergence test to verify our choice of element sizing parameters provide accurate Love number values on models with structural heterogeneities (see supplementary section S1.3 for details).

- For the *Base* models, we mesh a spherical shell with a specified input thickness $\tilde{d}_{ice}$. All of our models have baseline elastic parameters consistent with the rheology of ice (Jaccard, 1976; Shaw, 1985; Neumeier, 2018). We assign a base shear modulus value for ice of $G = 3.3$ GPa and a bulk modulus of $\mu = 8.6$ GPa (i.e., consistent with the formulation described in Souček et al., (2016) with $G = 3.3$ GPa and Poisson's ratio $\nu = 0.33$). For this analysis, we ignore viscous effects since viscous strain at the forcing period relevant for Enceladus (32.9 hours) is ex-

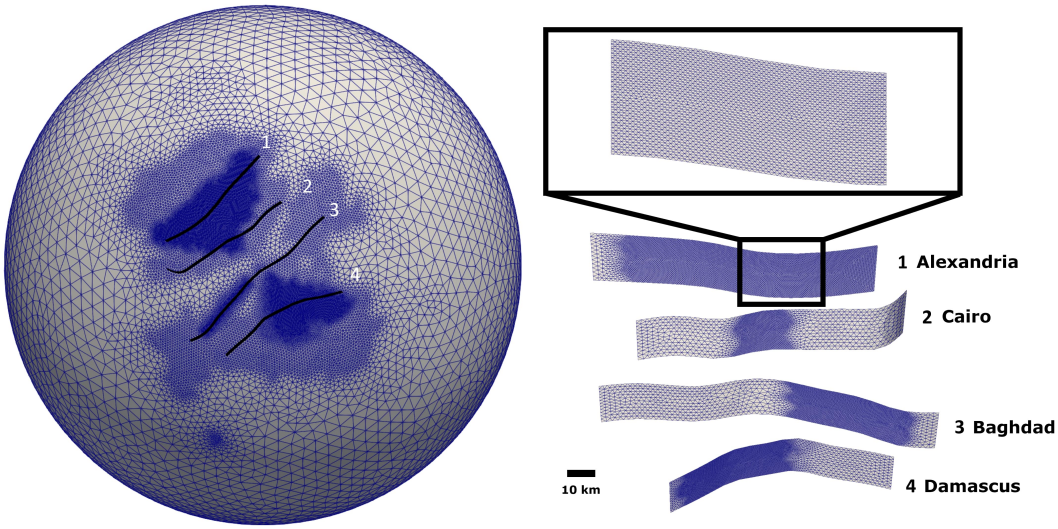

Figure 1. Example snapshots of mesh geometry from *Faulted* models (see main text). Left panel: South polar view of 3D mesh geometry discretized with tetrahedral elements. We refine cell sizes in regions that are expected to exhibit high strain upon tidal loading (in this case, near Tiger Stripes). The trace of the Tiger Stripes is shown as black lines on the outer surface of our geometry. Right panel: Perspective view of 2D discretization along Tiger Stripe surfaces. Inset image shows close-up view of mesh along Tiger Stripe 1 (i.e., Alexandria Sulcus). Labels for individual Tiger Stripes are shown in left and right panels. Cell edges are colored blue. An approximate distance scale is shown in the right panel for reference.

pected to be negligibly small (<1% of the total shell strain (Wahr et al., 2009), see also Supplemetary Section S1.6). Short-period elastic deformation of the core is also expected to be several orders of magnitude smaller than shell deformation (Schubert et al., 2007). We therefore treat the core as a rigid body and ignore any impact deformation of the core or related 3D mantle structures (e.g., ocean plumes driven by hydrothermal activity at the core-ocean boundary; Choblet et al., 2017) may have on the response of the ice shell to eccentricity tides.

- For the *Faulted* models, we introduce fault surfaces that are through-going (i.e., they extend through the full thickness of the ice shell) and are frictionless. The explicit inclusion of fault surfaces within the FEM formulation uses a 'split-node' formulation whereby we duplicate nodes along the fault plane and introduce special cohesive cells between node sets (Melosh & Raefsky, 2009; see also Supplementary S1.1). Split-node formulations allow for robust calculations of fault-induced

deformation and self-consistent predictions of fault slip. Our *Faulted* model specifically refers to a shell with four faults at the South Pole consistent with the mapped extent of Tiger Stripes at Enceladus. We extract the surface trace of the Tiger Stripes from existing maps of Enceladus (Schenk, 2008). We assume that effective hydrostatic normal stresses within water-filled cracks exceed extensional forces across fault geometries (Sládková et al., 2021 cf. Equation S14). We therefore ignore any potential impact of fault opening on deformation for *Faulted* models in this work (for details, see Supplementary S1.1).

- To construct the *LTV* models, we apply topography, H_{top}, to the outer surface of our base model geometry and modify the inner surface (i.e., the ice-ocean boundary), H_{bottom}, assuming isostatic (Airy) compensation. Given surface gravitational acceleration g_0, outer shell ice of density ρ_{ice}, ocean water of density ρ_w, gravitational acceleration at the ice-ocean interface g_{int}, mean radius of the outer surface R_0 (see Table 1 for chosen values of these parameters) (Hemingway & Matsuyama, 2017), and $\tilde{d}_{ice}$ we can write:

$$H_{bottom} = H_{top} \frac{\rho_{ice}}{(\rho_{ice} - \rho_w)} \frac{g_0}{g_{int}} \frac{R_0^2}{(R_0 - \tilde{d}_{ice})^2} \tag{6}$$

Table 1. Assumed parameter values used in Equation 6. Parameter values taken from Schenk et al., (2018)

Parameter	**Value**	**Units**
ρ_{ice}	925	kg/m^3
ρ_w	1007	kg/m^3
g_0	0.113	m/s^2
g_{int}	0.120	m/s^2
R_0	252.1	km

Our *LTV* models use topography extracted from the shape model given by Nimmo et al. (2011) up to a maximum spherical harmonic degree $L_{max} = 8$. Our *Faulted+LTV* model includes both types of structural heterogeneities.

- Our *WZ* models incorporate 1-km wide through-going 'weak zones' at locations corresponding to the south polar circum-tectonic boundary, chasma, and Tiger Stripes.

Yin & Pappalardo (2015), report that extensional, compressional, and shear stresses drive the formation of fractures in the circum-tectonic boundary surrounding the SPT whereas only extensional stresses appear to form the chasma that radiate away from the SPT. Although the fracture depth of faults observed at the circum-tectonic boundary and chasma remains poorly constrained based on current observations (Yin & Pappalardo, 2015), we would expect that all modes of fracture (extensional, compressional, and shear) in a finite-width volume would result in local 'damaged' regions of the ice shell which are less capable of accommodating tidally-driven stresses (i.e., exhibit a lower shear modulus) compared to the surrounding unfractured medium. In the most extreme feasible scenario, highly fractured regions of the crust (i.e., with porosity 0 % - 60%; we do not expect ice porosities $> 60\%$ due to pore compaction arising from hydrostatic confinement at depth; Durham et al., 2005) would penetrate to depths where liquid water from the subsurface ocean permeates the pore space of ice (Ingersoll & Nakajima, 2016). The pore pressure of fluid within a fractured ice matrix at depth within Enceladus's crust is not zero (i.e., the ice-water mixture exhibits 'undrained' conditions; Rovira-Navarro et al., 2022). The effective elastic bulk modulus for such a system is similar to the bulk modulus the solid ice phase (Rovira-Navarro et al., 2022 cf. Equation 18c). We therefore formulate weak zones as regions with an elastic shear modulus G_{WZ} reduced to negligible values $\sim 10^{-5}\,G$ but maintain a constant ice bulk modulus and density throughout our geometry.

Deformation driven by the presence of frictionless faults (i.e., 2D interfaces) is distinct from that arising from crustal weak zones (i.e., finite-width 3D volumes) in models. Water-filled fault interfaces subject to effective hydrostatic normal stresses that exceed tidally-driven stresses will resist extensional deformation in a manner similar to that of the surrounding elastic medium (see Supplementary S1.1.1.4; Sládková et al., 2021; Rovira-Navarro et al., 2022). By contrast, 3D volumes that contain weakened material will exhibit less resistance to normal stresses than the surrounding elastic medium due to a locally reduced elastic Young's modulus (i.e., which is sensitive to G_{WZ} for our formulation for weak zones; see also Segall, 2010). Reduced resistance to normal stresses along weak zones in WZ models should enable deformation patterns comparable to those expected from mode-1 crack opening (i.e., similar to the deformation produced by Tiger Stripes in Souček et al.,

2016). We do not consider the potentially distinct responses of highly fractured areas of the ice shell to extensional and compressional tidal stresses in this study. Our *Faulted+LTV+WZ* models incorporate weak zones, faults, and lateral variations in crustal thickness. Note that *Faulted+LTV+WZ* models in this work incorporate both 2D interfaces and 3D weak zones at Tiger Stripe locations.

2.2 Tidal Loading

For Enceladus, the driving potential (to the first order in eccentricity) produced by time-dependent eccentricity tides $V(r, \theta, \phi, t)$ at a point in a reference frame whose origin is fixed to Enceladus's center of mass (i.e., the ($\theta = 90°$, $\phi = 0°$) datum lies at the sub-Saturnian point, where θ is co-latitude and ϕ is longitude) is written as a combination of radial $V_{rad}(r, \theta, \phi, t)$ and librational $V_{lib}(r, \theta, \phi, t)$ terms (Murray & Dermott, 1999):

$$V_{rad}(r, \theta, \phi, t) = r^2 \omega^2 e \cdot \cos(\omega t) \, \frac{3}{4} \left(\mathrm{P}_{22}(\mu) \cos 2\phi - 2 \, \mathrm{P}_{20}(\mu) \right) \tag{7a}$$

$$V_{lib}(r, \theta, \phi, t) = r^2 \omega^2 e \cdot \sin(\omega t) \, \mathrm{P}_{22}(\mu) \sin 2\phi \tag{7b}$$

Each term in Equation 7 is scaled by the factor $\omega^2 e$, where $\omega = 5.307{\cdot}10^{-5}$ s^{-1} is Enceladus's orbital angular velocity and $e = 0.0047$ is the body's orbital eccentricity. Time $t = 0, \frac{2\pi}{\omega}$ corresponds to orbital periapse. $P_{20}(\mu)$ and $P_{22}(\mu)$ are associated Legendre Functions with the nested function $\mu = \cos(\theta)$. We apply body forces, ocean tractions, topographic surface traction forces, and self-gravitational forces produced by the driving potential from Equation 7 and calculate displacement fields arising from these loads. We ignore inertial forces for our analysis and obtain solutions for displacements at mesh nodes across the full 3D spherical geometry. We enforce zero rigid body rotations and translations for simulations (for details, see Supplementary 1.1).

We use the 3D visco-elasto-plastic FEM code PyLith (Aagaard et al., 2007). PyLith is a well-established and extensively benchmarked tool developed in the terrestrial crustal dynamics community for studying tectonic processes on Earth. PyLith allows for complex bulk rheology, various formulations for fault behavior, and complex geometrical meshes. PyLith was originally designed for quasi-Cartesian problems; as such we have modified it to allow for modeling full spheres in a no-net-rotation/translation reference frame with central time-dependent body forces appropriate for eccentricity tides. We benchmark our

tidal loading formulation as implemented in PyLith applied to our *Base* model against the program SatStress (Wahr et al., 2009) (see supplementary section S1.1-1.2).

2.3 Calculation of Love numbers

We post-process the resulting deformation fields to evaluate the $l = 2$ diurnal Love numbers k^d_{2m} and h^d_{2m}. The 'diurnal' Love numbers are distinct from 'fluid' Love numbers k^f_{2m} and h^f_{2m}. 'Fluid' Love numbers are sensitive to the arrangement of a body's interior layers which deflect in response to long-period static tides in order to achieve hydrostatic equilibrium (Goldreich & Mitchell, 2010). In contrast, diurnal Love numbers depend on the elastic response of the body to short-period eccentricity tides (see Equation 7) and are superimposed onto the long-period tide. Moreover, diurnal Love numbers are usually at least an order of magnitude smaller than fluid Love numbers (Beuthe, 2018; Hemingway & Mittal, 2019). Relative to the fluid Love numbers, the diurnal Love numbers are less sensitive to deeper interior structure at ocean worlds (Wahr et al., 2009).

For h^d_{2m}, we expand the outer surface of our deformed geometry into spherical harmonics and separately compute coefficients H_{2m}. We calculate V_{20}, V_{22}, and $V_{2\text{-}2}$ using the $l = 2$ components of the tidal potential from Equation 7:

$$V_{20} = -\frac{3}{2} r^2 \omega^2 e \cdot \cos(\omega t) \tag{8a}$$

$$V_{22} = \frac{3}{4} r^2 \omega^2 e \cdot \cos(\omega t) \tag{8b}$$

$$V_{2\text{-}2} = r^2 \omega^2 e \cdot \sin(\omega t) \tag{8c}$$

From V_{2m}, H_{2m}, and the definition of the effective Love numbers (see introduction), we have:

$$h^d_{2m} = g_0 H_{2m} / V_{2m} \tag{9}$$

Following a similar procedure for k^d_{2m}, we compute coefficients U_{2m} of the spherical harmonic expansion of the induced gravitational potential field (see Equation 1) associated with the deformed geometry:

$$k^d_{2m} = U_{2m} / V_{2m} \tag{10}$$

As mentioned earlier, Love numbers defined in this way will depend on the time-varying shape and amplitude of the driving potential (i.e., see Equations 4 and 8). Thus, we ex-

pect values of k^d_{2m} and h^d_{2m} to vary over the tidal cycle at Enceladus. Since we aim to minimize the impact of non-spherically symmetric structure on inferences of $\tilde{d}_{ice}$, we evaluate deformation at two unique points in the tidal cycle: $t = 0$ and $t = \frac{\pi}{2\omega}$. At $t = 0$ (or $\frac{\pi}{\omega}$), $V_{2\,\text{-}2} = 0$ (according to Equation 8) which eliminates the potential impact of the off-diagonal components $\gamma^{22}_{2\text{-}2}$, $\gamma^{20}_{2\text{-}2}$, $\gamma^{2}_{22}\text{-}^{2}$, and $\gamma^{2}_{20}\text{-}^{2}$ (from Equation 4) on values of k^d_{20} or k^d_{22}. Similarly, at $t = \frac{\pi}{2\omega}$ (or $\frac{3\pi}{2\omega}$), $V_{20} = V_{22} = 0$ which eliminates the impact of all off-diagonal components on values of $k^d_{2\text{-}2}$.

2.4 Ice Shell Thickness and Elastic Thickness

Mean ice shell thickness $\tilde{d}_{ice}$ described in our analysis is distinct from mean elastic thickness typically referenced in studies of plate flexure (e.g., Nimmo & Pappalardo, 2004; Conrad et al., 2019). Elastic thickness as inferred from flexure studies denotes the thickness of the crust that exhibits predominantly elastic (i.e., non-viscous) deformation over very long timescales (e.g., topographic loading; Mancktelow, 1999). For ocean world crusts, elastic thickness is typically a fraction ($< 70\%$) of the thermal thickness of the ice shell (i.e., the radial distance between the surface and the phase boundary between the ocean and the ice shell at 273 K). In contrast, $\tilde{d}_{ice}$ is the thickness of the ice shell that deforms elastically upon *cyclic* loading over diurnal timescales. Analyzing Love numbers from fully viscoelastic ice shells that are cyclically deformed over 32.9 hours periods produces estimates of $\tilde{d}_{ice}$ that are only slightly ($< 0.2\%$) larger than values of the thermal thickness of the crust at Enceladus (for details, see Supplementary S1.6).

2.5 Previous FEMs

Our FEMs are similar to, but distinct from, those described in the papers Souček et al., (2016), Behounkova et al., (2017), and Sládková et al., (2021). We employ a tidal forcing formulation which is identical to that described in Souček et al., (2016) to generate body, ocean traction, and topographic loading forces. However, we include the effect of self-gravitation in our models (which modifies final calculated values of k^d_{2m} and h^d_{2m} by up to 3%; Beuthe, 2018). Souček et al., (2016) employ weak zones (i.e., finite width regions with reduced elastic moduli) as proxies the behavior of fault interfaces. In contrast, we adopt a split-node approach at the fault-plane to simulate deformation which enables straightforward calculations of fault slip. Souček et al., (2016), Behounkova et al., (2017), and Sládková et al., (2021) also focus on the implications of deformation for

tidal heating, while we focus here on the inference of shell structural parameters in the presence of structural heterogeneities. Finally, our models additionally consider the effect of fault zones beyond the Tiger Stripes and thereby identify the extent to which other major structural heterogeneities (e.g., chasma and circum-tectonic boundaries) may affect diurnal deformation patterns at Enceladus.

The most significant difference between models by Souček et al., (2016) Behounkova et al., (2017), and Sládková et al., (2021) and those described in this work relates to respective formulations for weak zones. Souček et al., (2016) and Behounkova et al., (2017) reduce shear modulus to effectively negligible values while maintaining a constant Poisson's ratio within damaged regions. Such a formulation results in negligibly small values for weak zone bulk modulus. FEMs in Sládková et al., (2021) maintain constant weak zone elastic parameters but reduce viscosity within a finite-width volume to mimic static Coulomb friction along Tiger Stripes. Note that for zero static friction, the behavior of the Tiger Stripes in models by Sládková et al., (2021) approaches the behavior of weak zones in Souček et al., (2016) and Behounkova et al., (2017). The elastic moduli for weak zone formulations by Souček et al., (2016) and Behounkova et al., (2017) are consistent with those expected for a 'drained' two-phase system (Rovira-Navarro et al., 2022 cf. Equation 18b). We expect that 'undrained' conditions exist for ice-water mixtures subject to hydrostatic pressures at depth (Rovira-Navarro et al., 2022; Sládková et al., 2021). We therefore choose to maintain a constant bulk modulus in weak zones for this work (see previous discussion in section 2.1 for *WZ* models). Note that we are able to broadly reproduce the results of Souček et al., (2016) by employing weak zones only at Tiger Stripe locations and reducing both bulk and shear modulus to effectively negligible values in Supplementary S1.2.

3 Results

Figures 2 and 3 show snapshots of the radial displacement fields from each of the six model classes. The upper panels show absolute displacements on our *Base* model whereas the subsequent panels show the radial displacement fields for models incorporating structural heterogeneities relative to our *Base* model. Not surprisingly, there is a substantial increase in localized deformation near zones of structural heterogeneities (i.e., broadly consistent with model results from Souček et al.,2016; Behounkova et al., 2017; and Sládková et al., 2021). For the *LTV* model, we find that the highest increases in displacement val-

ues occur near the South Pole where the ice shell is thinnest. In the *Faulted* model, radial displacements are maximum near fault tips (also at the South Pole). In our *WZ* and *Faulted+LTV+WZ* model, localized radial deformation is partitioned between the Tiger Stripes, chasma, and circum-tectonic boundaries in a complex manner with further increases in displacement near the Tiger Stripes due to extensional and shear strain localization along weak zones. Note that the addition of lateral variations in crustal thickness alters the geometry of weak zones in *Faulted+LTV+WZ* models relative to those in *WZ* models resulting in distinct displacement fields produced by weak zones in either case. Long-wavelength increases in displacement amplify values of the Love numbers for all models that incorporate structural heterogeneities. Moreover, surface deformation at this scale does not follow the pattern of the disturbing potential from Equation 7. This difference causes values of k^d_{20}, k^d_{22}, and $k^d_{2\text{-}2}$ (or h^d_{20}, h^d_{22}, and $h^d_{2\text{-}2}$) to diverge from each other (i.e., 'order-splitting').

Figure 4 shows additional snapshots of fault slip along the Tiger Stripes as evaluated by our *Faulted* model and crustal thickness variations in our *LTV* model. Displacements surrounding the South Pole in the *Faulted* model follow a double-couple pattern (i.e., a symmetric pattern of alternating maximal and minimal radial displacement around the fault tips; Segall, 2010) consistent with left-lateral strike-slip motion observed along the Tiger Stripes in Figure 4. Regional thinning at the North and South Poles in our *LTV* model also drive quadrupole displacement patterns across Northern and Southern hemispheres. However, the higher amplitude and greater regional extent of crustal thinning at the SPT (i.e., compared to that near the North Pole) results in relatively higher radial displacements over the Southern Hemisphere in *LTV* models.

Our *Faulted*, *Faulted+LTV*, *WZ*, and *Faulted+LTV+WZ* models predict significantly lower localized displacement along the length Tiger Stripes (i.e., $\sim$ 20 cm) than do FEMs by Souček et al., (2016) and Behounkova et al., (2017) ($\sim$ 1-7 m). In the case of *Faulted* and *Faulted+LTV* models, the effect of clamping opening and closing motion across fault structures (see Supplementary S1.1) suppresses mode-1 deformation surrounding Tiger Stripes (Segall, 2010). In contrast, reducing the shear modulus along weak zones in *WZ* and *Faulted+LTV+WZ* models produces discontinuities in radial displacement across the Tiger Stripes similar to those produced by mode-1 crack opening displacement (Segall, 2010). However, the inclusion of a non-zero bulk modulus in weak zones for *WZ* and *Faulted+LTV+WZ* models reduces the magnitude of extensional and compressional strain over the Tiger Stripes

as compared to the predicted impact of weak zones in FEMs by Souček et al., (2016) (see sections 2.1 and 2.5 of the methods for details).

Results for k^d_{20}, h^d_{20}, $k^d_{2\text{-}2}$. and $h^d_{2\text{-}2}$ from each model category are shown in Figure 5. Results similar to those shown in Figure 5 illustrating the behavior of k^d_{22} and h^d_{22} are also shown in Figure 6. Note that non-spherically symmetric models have enhanced values of Love numbers across all $\tilde{d}_{ice}$ values consistent with the amplification of deformation shown in models with structural heterogeneities (see Figures 2 and 3). Love number results in Figures 5 and 6 imply that inferences of elastic structure which assume Enceladus is spherically symmetric (i.e., the *Base* model) will underestimate $\tilde{d}_{ice}$ if structural heterogeneities are present in the crust. To evaluate this model error, $\Delta\%\tilde{d}_{ice}$, we determine the percentage difference between $\tilde{d}_{ice}$ assigned to the *Base* models and the mean thickness of selected models with heterogeneities (i.e., $\tilde{d}^{Het}_{ice}$) which each produce the same value of h^d_{2m} or k^d_{2m}:

$$\Delta\%\tilde{d}_{ice} = \frac{\tilde{d}^{Het}_{ice} - \tilde{d}_{ice}}{\tilde{d}_{ice}} \cdot 100\%. \tag{11}$$

Figures 5 and 6 show $\Delta\%\tilde{d}_{ice}$ for each model category with structural heterogeneities. Results demonstrate that Tiger Stripes in the *Faulted* models minimally ($< 3\%$) impact values of $\Delta\%\tilde{d}_{ice}$. By contrast, weak zones and variations in crustal thickness (in *WZ* and *LTV* models) bias inferences of $\tilde{d}_{ice}$ from Love numbers by up to $\sim 18\%$ and $\sim 20\%$ respectively. The most extreme case (*Faulted+LTV+WZ* models) yields values of $\Delta\%\tilde{d}_{ice}$ as high as $\sim 41\%$. Small differences between the shape of h^d_{2m} or k^d_{2m} curves (and $\Delta\%\tilde{d}_{ice}$ curves evaluated from h^d_{2m} or k^d_{2m}) arise from slight differences in radial displacement patterns at the outer surface and the ice-ocean boundary across models.

Note the distinct values of k^d_{22} and h^d_{22} compared to k^d_{20} and h^d_{20} or $k^d_{2\text{-}2}$ and $h^d_{2\text{-}2}$ (i.e., 'order-splitting') in models with structural heterogeneities in Figures 5 and 6. To directly quantify the impact of structural heterogeneities on order-splitting, we additionally plot values of k^d_{22}/k^d_{20} and h^d_{22}/h^d_{20} vs. $\tilde{d}_{ice}$ in Figure 6. We track k^d_{22}/k^d_{20} and h^d_{22}/h^d_{20} since these quantities implicitly account for the baseline impact of $\tilde{d}_{ice}$ on Love numbers and are especially sensitive to the presence of structural heterogeneities near the South Pole of Enceladus (see discussion).

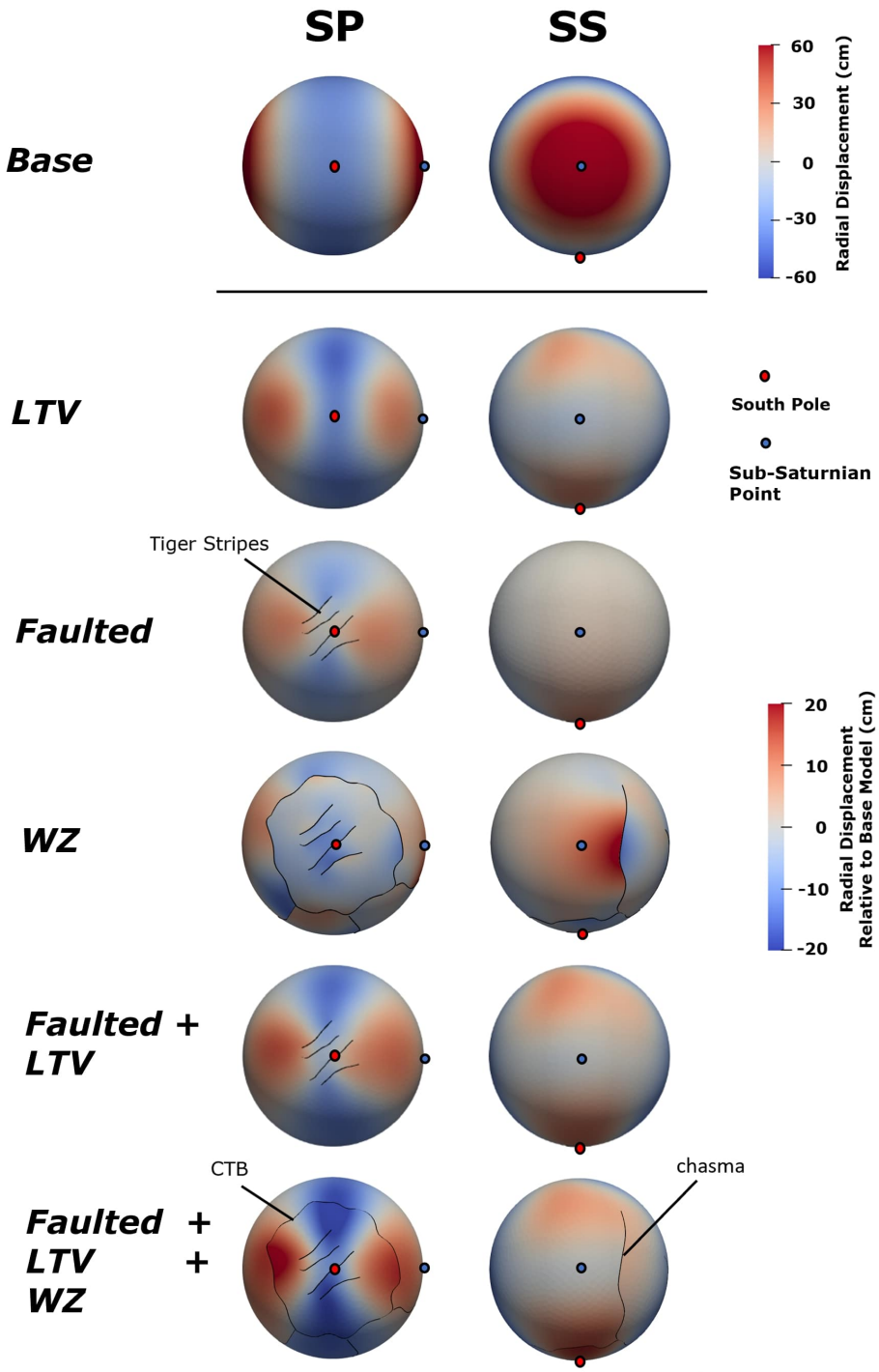

Figure 2. Snapshots of radial displacement from each model class viewed facing the South Pole (SP, left column) and the sub-Saturnian point (SS, right column) evaluated at $t = 0$ (periapse). The top row shows the radial displacement in the *Base* model due to tidal forcing. The remaining rows present the differences in radial displacement between models with structural heterogeneities and the *Base* model. Each model shown assumes $\tilde{d}_{ice} = 25$ km. Tiger Stripes, the south polar circum-tectonic boundary (CTB), and chasma are labelled. Figure 3 shows the same models at a different time in Enceladus's orbit. To view model results for horizontal displacements at $t = 0$, refer to Supplementary S1.7.

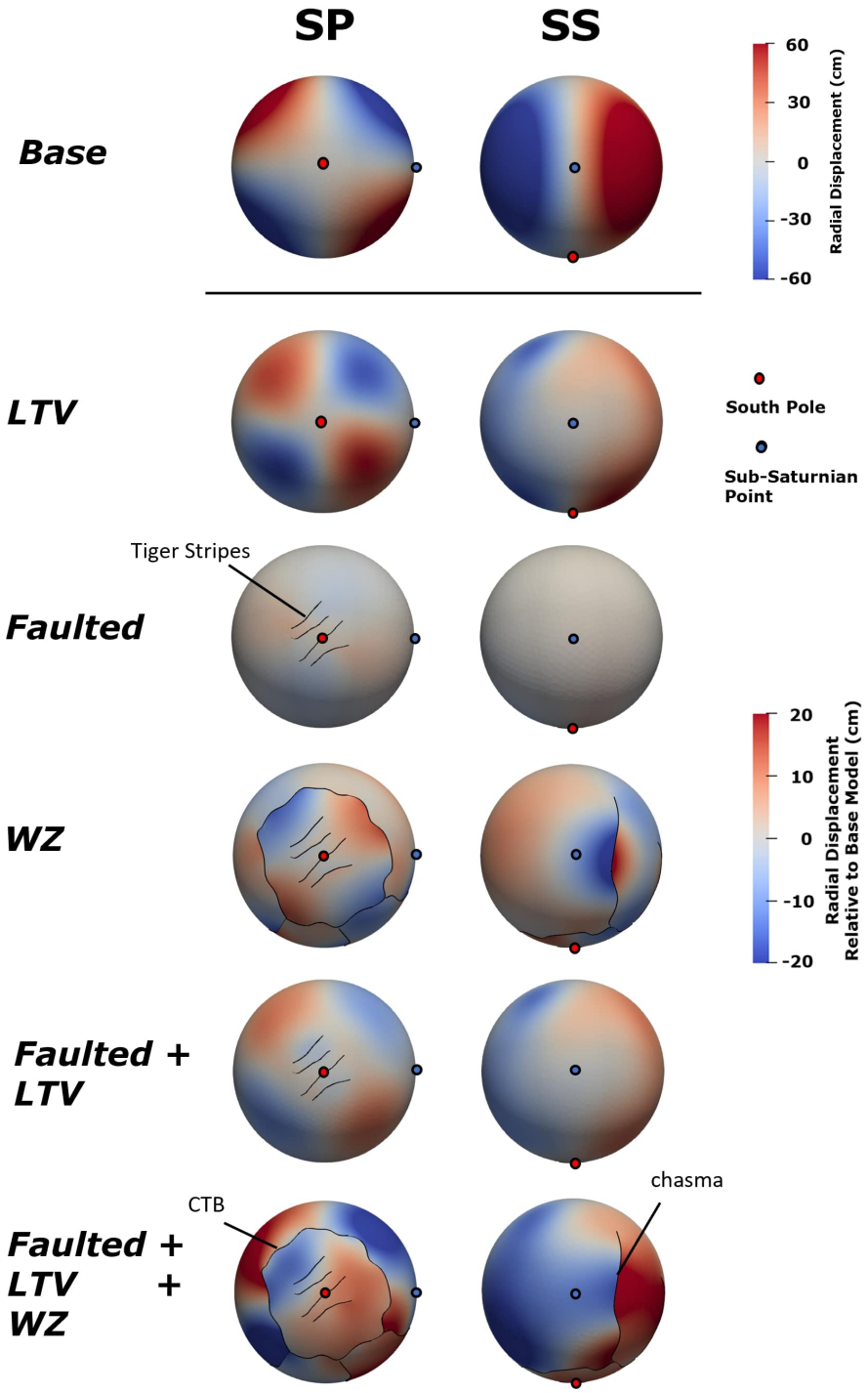

Figure 3. Snapshots of radial displacement from each model class viewed facing the South Pole (SP, left column) and the sub-Saturnian point (SS, right column) evaluated at $t = \frac{\pi}{2\omega}$. The top row shows the radial displacement in the *Base* model due to tidal forcing. The remaining rows present the differences in radial displacement between models with structural heterogeneities and the *Base* model. Each model shown assumes $\tilde{d}_{ice} = 25$ km. Tiger Stripes, the south polar circum-tectonic boundary (CTB), and chasma are labelled. Figure 2 shows the same models at a different time in Enceladus's orbit.

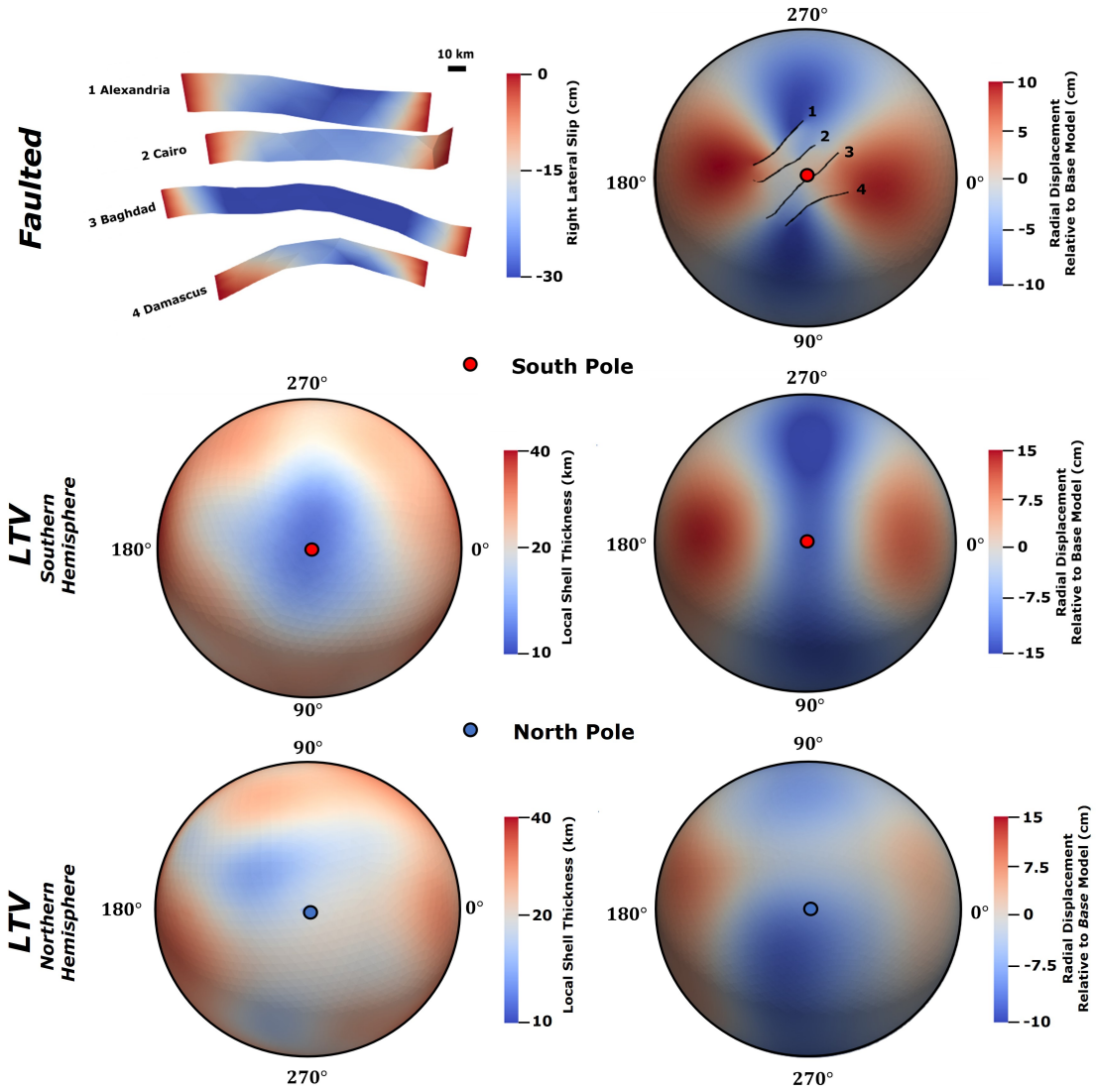

Figure 4. Snapshots of slip along the Tiger Stripes and regional thinning respectively corresponding to deformation shown in *Faulted* (top row) and *LTV* (center and bottom rows) models in Figure 2. The upper left image shows a perspective view of fault slip on the Tiger Stripes, where negative (blue) values indicate left-lateral slip. The upper right shows a south polar projection (where 0° corresponds to the sub-Saturnian longitude), with fault locations overlaid on radial displacements (this is rescaled from the third row of Figure 2). The center and bottom rows respectively show images of polar projections showing crustal thickness variations (left) and radial displacements (right) evaluated from the *LTV* model (i.e., rescaled from the second row of Figure 2) in the Northern and Southern Hemispheres. Local thickness values are plotted in $\log_{10}$ scale. Each model shown assumes $\tilde{d}_{ice} = 25$ km and is evaluated at $t = 0$ (periapse). South and North Poles marked for reference. Longitude labels denote degrees East of the sub-Saturnian point. See Supplementary Figure S8 or an additional plot of crustal thickness variations used for *LTV* models.

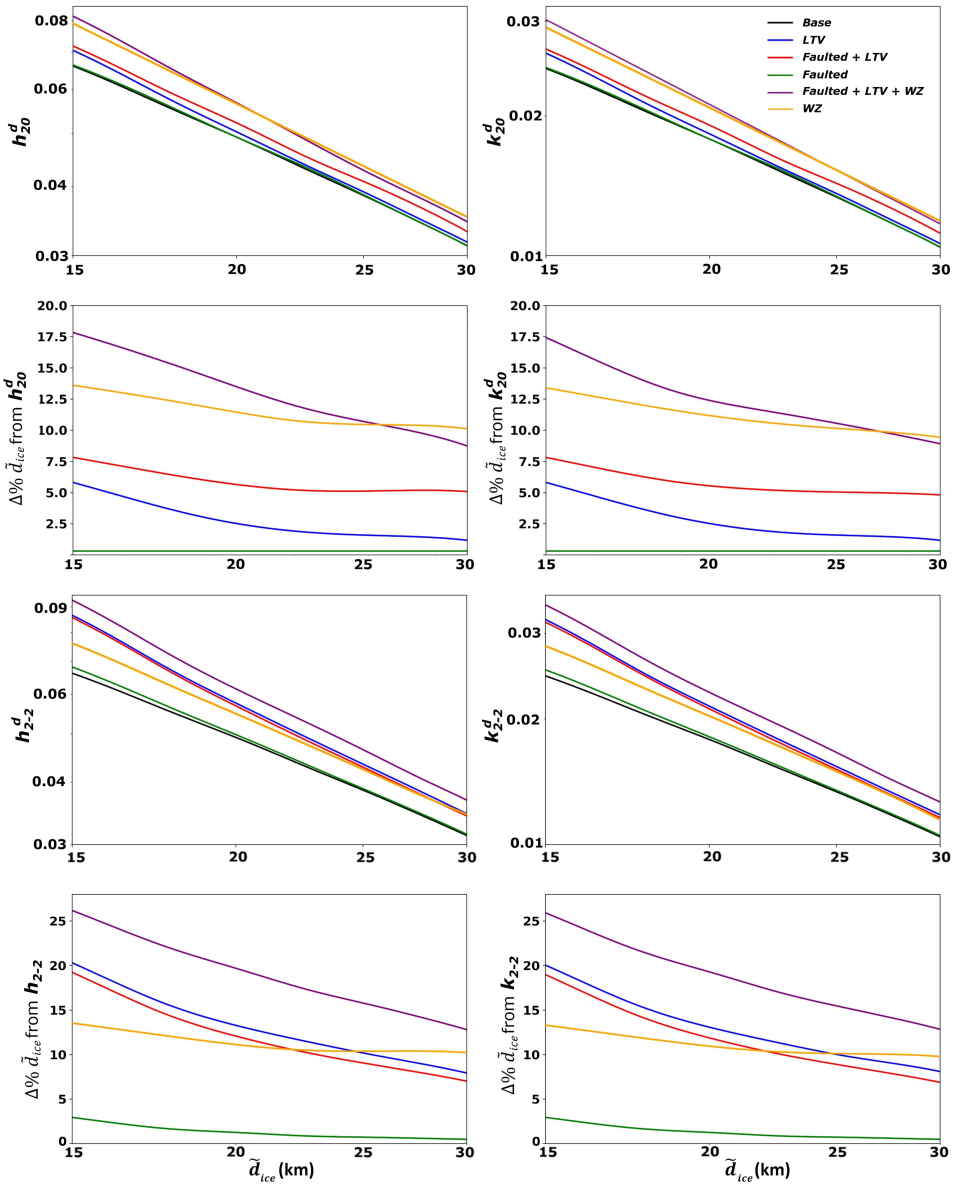

Figure 5. The relationship between deformation and mean ice shell thickness, $\tilde{d}_{ice}$. First row: h^d_{20} and k^d_{20} vs. $\tilde{d}_{ice}$ for *Base* models (black lines), *LTV* models (blue lines), *Faulted* models (red lines), *Faulted+LTV* models (green lines), and *Faulted+LTV+WZ* (purple lines). We plot both axes in $\log_{10}$ scale and generate curves by evaluating h^d_{20} and k^d_{20} at t=0 (periapse) for 40 equally spaced $\tilde{d}_{ice}$ values between 15 and 30 km. Second row: Percentage range of $\tilde{d}_{ice}$ values corresponding to a fixed Love number values for each model category relative to the *Base* model. Curves in these plots are generated by evaluating $\Delta\%\tilde{d}_{ice}$ from Equation 11. X-axes are plotted in $\log_{10}$ scale. Third and Fourth Rows: similar to first and second rows (respectively) but for $h^d_{2\text{-}2}$ and $k^d_{2\text{-}2}$ evaluated at $t = \frac{\pi}{2\omega}$.

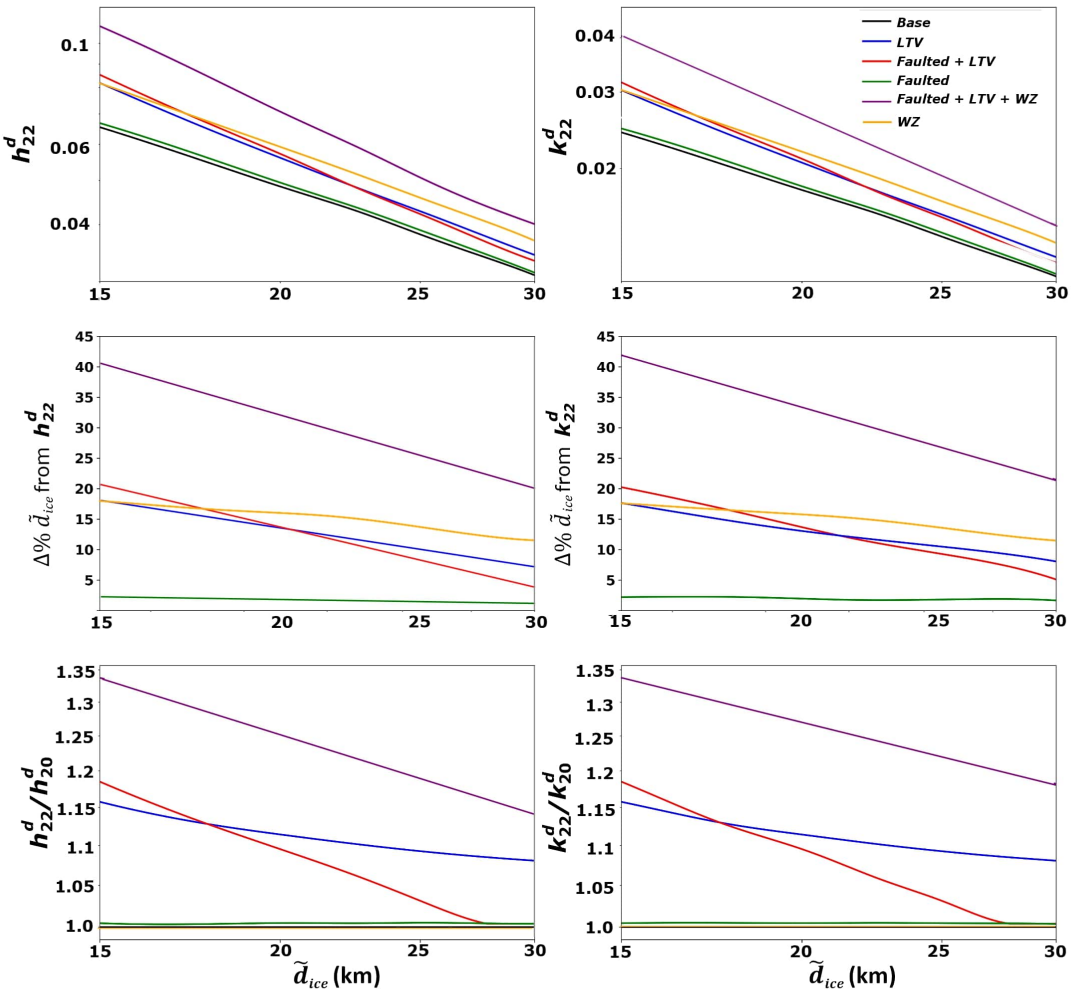

Figure 6. First row: Similar to first row of Figure 5 but for h^d_{22} and k^d_{22} instead of h^d_{20} and k^d_{20}. Second row: Similar to second row of Figure 5 for h^d_{22} and k^d_{22} instead of h^d_{20} and k^d_{20}. Third Row: 'order-splitting' associated with $l = 2$ Love numbers. We evaluate k^d_{22} and h^d_{22} or k^d_{20} and h^d_{20} at t=0 (periapse) for 40 equally spaced $\tilde{d}_{ice}$ values between 15 and 30 km to compute k^d_{22}/k^d_{20} and h^d_{22}/h^d_{20}. X-axes are plotted in $\log_{10}$ scale.

4 Discussion

We explore the dependence of diurnal Love number values on the presence of structural heterogeneities and $\tilde{d}_{ice}$ at Enceladus. Of the simplified structural heterogeneities considered, weak zones appear to have the most significant impact on the diurnal response of the ice shell to tides across the range of possible $\tilde{d}_{ice}$ (15–30 km) at Enceladus. The large spatial extent of the weak zones (i.e., 200–500 km in length or comparable to the radial length scale of Enceladus) and capacity to accommodate both additional normal- and shear-strain drives higher Love number values than those produced from the presence of variations in the thickness of the crust and faults in isolation. We find that for cases with less pronounced weak zones (i.e., where $G_{WZ}/G > 10^{-5}$), the amplification of deformation drops dramatically (see Supplementary section S1.4 for details). These findings are consistent with results from Souček et al., (2016) and Behounkova et al., (2017) despite differences in the implementation of weak zones between the respective models (see section 2.4).

The diurnal response of Enceladus to eccentricity tides is also highly sensitive to variations in the thickness of the ice crust. *LTV* models show deviation in inferred $\tilde{d}_{ice}$ values relative to *Base* models of up to 20%. The amplification of deformation in thinned regions (see Figures 2 and 4) is highly dependent on $\tilde{d}_{ice}$. As $\tilde{d}_{ice}$ approaches 15 km, ice shell thickness approaches zero locally and strain increases rapidly near the South Pole. The resulting enhanced deformation drives the observed large increase in Love numbers at $\tilde{d}_{ice} < 20$ km (Figure 5 and 6).

As implemented here, faults have less impact on long-wavelength deformation than do variations in the thickness of the ice crust or weak zones. Fault structures in isolation bias inferred $\tilde{d}_{ice}$ values from diurnal Love number values by up to 3%—rather insignificant. This observation follows from Figures 2 and 4 which shows that fault-induced deformation creates a strong double-couple deformation pattern as expected from slip on Tiger Stripes. Slip-induced deformation produces substantial radial displacement at scales comparable to the size of associated faults but reduced displacement at longer wavelengths. As such, for the Tiger Stripes along-fault slip only modestly increases diurnal Love number values. Moreover, we expect the influence of Tiger Stripe slip on diurnal Love number values to decrease as maximum principal stresses rotate around the South Pole and fault slip decreases (see Figure 3).

493 We find significant order-splitting (i.e., $k_{22}^d/k_{20}^d \neq 1$ and $h_{22}^d/h_{20}^d \neq 1$) in models
494 with structural heterogeneities. Moreover, Figures 2 and 6 suggest k_{22}^d/k_{20}^d and h_{22}^d/h_{20}^d
495 are highly sensitive to the scale of non-spherically symmetric structure near the South
496 Pole. For *LTV* models, radial displacement patterns exhibit strong, long-wavelength quadrupole
497 symmetry about the South Pole (i.e., generating an $m = 2$ pattern) causing larger val-
498 ues of k_{22}^d/k_{20}^d and h_{22}^d/h_{20}^d. In contrast, slip along Tiger Stripe faults produces shorter-
499 wavelength quadrupole deformation resulting in relatively smaller values of k_{22}^d/k_{20}^d and
500 h_{22}^d/k_{20}^d. In *Faulted+LTV* models, slip-induced short wavelength deformation dominantly
501 accommodates strain when $\tilde{d}_{ice}$ >25 km (i.e., resulting in k_{22}^d/k_{20}^d values trending to-
502 wards 1, whereas at smaller values of $\tilde{d}_{ice}$, the effect of LTVs dominate such that k_{22}^d/k_{20}^d
503 and $h_{22}^d/h_{20}^d >> 1$). Weak zones combined with lateral variations in thickness (i.e., in
504 *Faulted+LTV+WZ* models) produce the highest levels of quasi-quadrupole deformation
505 near the South Pole and so drive the largest values of k_{22}^d/k_{20}^d and h_{22}^d/h_{20}^d (up to ~ 1.35
506 or 35%).

507 The non degree-2 deformation patterns visible for our range of models (see Figures
508 2 - 4) implies that significant mode coupling occurs when structural heterogeneities are
509 present in the crust of Enceladus (see Introduction; Qin et al., 2014; Zhong et al., 2021;
510 Lau et al., 2015). Consistent with Love number results in Figures 5 - 6, we find that the
511 lateral extent of structural heterogeneities scales with the spatial wavelength of non degree-
512 2 deformation (see Supplementary S1.5 for details). We expect that spatial variations
513 in the rheological properties along faults or weak zones (e.g., changes in the shear mod-
514 ulus, the coefficient of static friction) complicate inferences of $\tilde{d}_{ice}$ from non-degree 2 tidal
515 deformation produced by these structures. However, the impact of lateral variations in
516 crustal thickness on displacement fields (e.g., Love numbers and mode coupling) is more
517 uniquely sensitive to $\tilde{d}_{ice}$ at Enceladus (see previous discussion and Figures 5 and 6). In-
518 ferring both $\tilde{d}_{ice}$ and lateral variations in crustal thickness from deformation evaluated
519 across multiple spatial wavelengths is therefore a compelling topic for future research,
520 but is beyond the scope of the current work.

521 The predicted amplitude of tidally-driven radial surface displacements falls within
522 a readily measurable range at Enceladus. Figures 2, 3, 5, and 6 show that the maximum
523 amplitude of the time-variable component of radial surface displacement is approximately
524 50 – 150 cm, with differences of 5 – 20 cm between models. The maximal values for the
525 time-variable components of horizontal displacement also differ between models, with

a range of 15 – 20 cm relative to background values of about 5 – 10 cm near the South Pole (see Supplementary S1.7). These values are substantially larger than the demonstrated sensitivity of Interferometric Synthetic Apreture Radar (InSAR) to measurements of ground displacement (e.g., Simons & Rosen, 2015). Moreover, radial surface displacements of 5 – 20 cm can induce 2 – 80 μGal time-variable gravity anomalies which is greater than the expected detection limit of gravity measurements acquired from line-of-sight tracking between multiple orbiting spacecraft (e.g., Ramillien et al., 2004 and Dai et al., 2016). An orbiting spacecraft capable of repeated geodetic measurements over several months could gather snapshots of gravity and the radial position of the surface at multiple points over Enceladus. This data could be analyzed to create a quasi-continuous time-series of geodetic signals over the body, enabling computation of h^d_{2m} and k^d_{2m}. Therefore, a dedicated geodetic mission to Enceladus could be envisioned to acquire the necessary measurements for analyzing diurnal tides as discussed in this work.

We ignore the potential impact of lateral variations in elastic moduli on tidal deformation. However, the elastic shear modulus of ice in Enceladus's crust is sensitive to the ~ 40°K elevated temperature over the SPT (Howett et al., 2010). A ~ 40 K temperature variation corresponds to a change in ice shear modulus of about 2 - 3% (Proctor, 1966; Neumeier, 2018). For comparison, variations in crustal thickness of up to 100% of $\tilde{d}_{ice}$ near the SPT in LTV model alters Love numbers by up to $\sim 20\%$ (see Figures 5 - 6). The impact of variations in elastic shear modulus on Love numbers is similar to that corresponding to the presence of lateral variations in crustal thickness (Wahr et al., 2006 cf. Equation 4-9). We therefore expect that variations in shear modulus of 2 - 3% over the SPT induce ~ 0.1 - 0.2% (i.e., essentially negligible) differences in Love number values for Enceladus.

We assume a density structure for the crust and ocean (see Table 1), however the ocean density, ρ_w, is particularly uncertain. This uncertainty biases inferred values of $\tilde{d}_{ice}$ derived from diurnal Love numbers since ρ_w scales the restoring force at the ice-ocean interface (see section 2.2 and supplementary S1.1). Uncertainties in estimates of ρ_w are approximately 5% (i.e., $\rho_w = 1000$–1050 kg/m^3; Čadek et al., 2016) and thus uncertainty in ρ_w can modify diurnal Love numbers by up to 4%. Propagated uncertainty from imprecise estimates of ρ_w is therefore slightly larger than model uncertainty associated with the presence of Tiger Stripes (3%) but substantially smaller than that produced from neglecting the potential influence of weak zones or variations in ice shell thickness. More-

over, changing the input value of ρ_w should not produce order-splitting and so does not alter inferences short-wavelength shell structure from comparisons of diurnal Love numbers.

Spherically symmetric (i.e., 1D) models for tidal deformation can adequately describe the relationship between Love numbers and $\tilde{d}_{ice}$ for many ocean worlds (Wahr et al., 2006). For example, Europa and Ganymede exhibit relatively small amplitudes of lateral variations in crustal thickness ($\sim$ a few km) compared to likely mean thickness values $>$ 20 km (McKinnon & Melosh, 1980; Howell, 2021). These two worlds also lack discernible large-scale fault structures or weak zones (Hoppa et al., 2000; McKinnon & Melosh, 1980; Cameron et al., 2019). As such, the use of 3D models to improve estimates of $\tilde{d}_{ice}$ is not necessary for these bodies since the inherent uncertainty posed by imperfect estimates of bulk structure (e.g., ocean density, Nimmo et al., 2007) is likely to outweigh that arising from the presence of structural heterogeneities. In contrast, structural heterogeneities at Enceladus drive a $\sim$20-40% change in Love numbers which is much greater than the previously discussed $<$ 5% uncertainty posed by the impact of uncertainty in ocean density or elastic moduli (Howett et al., 2010; Čadek et al., 2016). Thus, 3D models are crucial for using tidal deformation to characterize $\tilde{d}_{ice}$ at Enceladus.

5 Conclusion

We evaluate the relationship between mean ice shell thickness, $\tilde{d}_{ice}$, and diurnal Love numbers for a range of shell models with structural heterogeneities. We find that structural heterogeneities at Enceladus broaden the range of possible $\tilde{d}_{ice}$ values corresponding to a measured Love number by about 41% in the most extreme case. The maximal range of plausible $\tilde{d}_{ice}$ values increases less than 30% for $\tilde{d}_{ice}$ values above 20 km (likely values of $\tilde{d}_{ice}$ at Enceladus are between 21–26 km; Thomas et al., 2016). Moreover, if weak zones are not present then the range of plausible $\tilde{d}_{ice}$ values further reduces to less than $\sim$ 20%. As such, we demonstrate that analysis of diurnal tides could serve as a useful tool for characterizing interior structure from future geodetic investigations at Enceladus.

Open Research

The data used in this study were generated using the software package PyLith (Aagaard et al., 2007; Aagaard et al., 2022). PyLith is an open-source finite element code

for modeling geodynamic processes and is available on GitHub and Zenodo repositories (Aagaard et al., 2022). The specific PyLith version used in this study was v2.2.2. PyLith input files, post-processing scripts, and selected output files for this work are available on (Berne, 2023). The mesh geometries utilized in this study were created using CUBIT (v15.2), a node-locked licensed software which is available through the developer Sandia National Laboratories (Skroch et al., 2019; CoreForm, 2020).

Acknowledgments

We would like to express our gratitude to the reviewers and editors for their valuable contributions in improving the clarity and content of this manuscript. This research was supported by the Future Investigators in NASA Earth and Space Science and Technology (FINESST) Program (80NSSC22K1318). We also thank the Keck Institute for Space Studies (KISS) at California Institute of Technology for organizing two workshops about "Next-Generation Planetary Geodesy" which provided insight, expertise, and discussions that greatly assisted the research. We also thank Matthew Knepley, Brad Aagaard, and Charles Williams for providing invaluable advice to modify PyLith for the simulations described this work. A portion of this research was supported by a Strategic Research and Technology Development task led by James T. Keane and Ryan S. Park at the Jet Propulsion Laboratory, California Institute of Technology, under a contract with the National Aeronautics and Space Administration (80NM0018D0004).

References

Aagaard, B., Williams, C., & Knepley, M. (2007). PyLith: A Finite-Element Code for Modeling Quasi-Static and Dynamic Crustal Deformation. *Eos*, *88(52)*.

Aagaard, B., Williams, C., & Knepley, M. (2022). PyLith: A Finite-Element Code for Modeling Quasi-Static and Dynamic Crustal Deformation. *geodynamics/pylith v2.2.2 (v2.2.2) [Computer software]. Zenodo,https://doi.org/10.5281/zenodo.3269486*, .

Aki, K., & Richards, P. (1981). K. aki and p. g. richards 1980. quantitative seismology, theory and methods. volume i: 557 pp., 169 illustrations. volume ii: 373 pp., 116 illustrations. san francisco: Freeman. price: Volume i, u.s. 35.00; *volumeii*, *u.s.*35.00. isbn 0 7167 1058 7 (vol. i), 0 7167 1059 5 (vol. ii). *Geological Magazine*, *118*. doi: 10.1017/s0016756800034439

Akiba, R., Ermakov, A. I., & Militzer, B. (2022). Probing the icy shell structure of ocean worlds with gravity–topography admittance. *The Planetary Science Journal*, *3*. doi: 10.3847/psj/ac4d2b

Behounkova, M., Soucek, O., Hron, J., & Cadec, O. (2017). Plume activity and tidal deformation on enceladus influenced by faults and variable ice shell thickness. *Astrobiology*, *17*(9). doi: 10.1089/ast.2016.1629

Berne, A. (2023). *acberne/Berne_2023_Pylith_Input_Files: Pylith input files and selected outputs for Berne et al., 2023 (v1.0.0).* `https://doi.org/10.5281/zenodo.7779514`. Zenodo.

Beuthe, M. (2018). Enceladus's crust as a non-uniform thin shell: I tidal deformations. *Icarus*, *302*. doi: 10.1016/j.icarus.2017.11.009

Cameron, M. E., Smith-Konter, B. R., Collins, G. C., Patthoff, D. A., & Pappalardo, R. T. (2019). Tidal stress modeling of Ganymede: Strike-slip tectonism and Coulomb failure. *Icarus*, *319*. doi: 10.1016/j.icarus.2018.09.002

Choblet, G., Tobie, G., Sotin, C., Běhounková, M., Čadek, O., Postberg, F., & Souček, O. (2017). Powering prolonged hydrothermal activity inside enceladus. *Nature Astronomy*, *1*. doi: 10.1038/s41550-017-0289-8

Conrad, J. W., Nimmo, F., Schenk, P. M., McKinnon, W. B., Moore, J. M., Beddingfield, C. B., ... Ennico, K. (2019). An upper bound on pluto's heat flux from a lack of flexural response of its normal faults. *Icarus*, *328*. doi: 10.1016/j.icarus.2019.03.028

CoreForm. (2020). "CUBIT" https://coreform.com/products/coreform-cubit/ .

Dahlen, F. A., & Tromp, J. (1998). *Theoretical global seismology.* doi: 10.1063/1.882788

Dai, C., Shum, C. K., Guo, J., Shang, K., Tapley, B., & Wang, R. (2016). Improved source parameter constraints for five undersea earthquakes from north component of GRACE gravity and gravity gradient change measurements. *Earth and Planetary Science Letters*, *443*. doi: 10.1016/j.epsl.2016.03.025

Durham, W. B., McKinnon, W. B., & Stern, L. A. (2005). Cold compaction of water ice. *Geophysical Research Letters*, *32*. doi: 10.1029/2005GL023484

Ermakov, A. I., Park, R. S., Roa, J., Castillo-Rogez, J. C., Keane, J. T., Nimmo, F., ... Lainey, V. (2021). A recipe for the geophysical exploration of enceladus. *Planetary Science Journal*, *2*. doi: 10.3847/PSJ/ac06d2

Friedson, A. J., & Stevenson, D. J. (1983). Viscosity of rock-ice mixtures and applications to the evolution of icy satellites. *Icarus*, *56*. doi: 10.1016/0019-1035(83)90124-0

Goldreich, P. M., & Mitchell, J. L. (2010). Elastic ice shells of synchronous moons: Implications for cracks on europa and non-synchronous rotation of titan. *Icarus*, *209*. doi: 10.1016/j.icarus.2010.04.013

Hansen, C. J., Esposito, L., Stewart, A. I., Colwell, J., Hendrix, A., Pryor, W., & Wast, R. (2006). Enceladus' water vapor plume. *Science*, *311*. doi: 10.1126/science.1121254

Hay, H. C., & Matsuyama, I. (2019). Nonlinear tidal dissipation in the subsurface oceans of enceladus and other icy satellites. *Icarus*, *319*. doi: 10.1016/j.icarus.2018.09.019

Hemingway, D. J., & Matsuyama, I. (2017). Isostatic equilibrium in spherical coordinates and implications for crustal thickness on the Moon, Mars, Enceladus, and elsewhere. *Geophysical Research Letters*, *44*(15). doi: 10.1002/2017GL073334

Hemingway, D. J., & Mittal, T. (2019). Enceladus's ice shell structure as a window on internal heat production. *Icarus*, *332*. doi: 10.1016/j.icarus.2019.03.011

Hoppa, G., Greenberg, R., Tufts, B. R., Geissler, P., Phillips, C., & Milazzo, M. (2000). Distribution of strike-slip faults on Europa. *Journal of Geophysical Research E: Planets*, *105*(E9). doi: 10.1029/1999JE001156

Howell, S. M. (2021). The likely thickness of europa's icy shell. *Planetary Science Journal*, *2*(4). doi: 10.3847/PSJ/abfe10

Howett, C. J., Spencer, J. R., Pearl, J., & Segura, M. (2010). Thermal inertia and bolometric bond albedo values for mimas, enceladus, tethys, dione, rhea and iapetus as derived from cassini/cirs measurements. *Icarus*, *206*. doi: 10.1016/j.icarus.2009.07.016

Hubbard, W. B., & Anderson, J. D. (1978). Possible flyby measurements of galilean satellite interior structure. *Icarus*, *33*. doi: 10.1016/0019-1035(78)90153-7

Hurford, T. A., Helfenstein, P., Hoppa, G. V., Greenberg, R., & Bills, B. G. (2007). Eruptions arising from tidally controlled periodic openings of rifts on enceladus. *Nature*, *447*. doi: 10.1038/nature05821

Iess, L., Stevenson, D. J., Parisi, M., Hemingway, D., Jacobson, R. A., Lunine, J. I., & Tortora, P. (2014). The gravity field and interior structure of Enceladus.

Science, *344*(6179). doi: 10.1126/science.1250551

Ingersoll, A. P., Ewald, S. P., & Trumbo, S. K. (2020). Time variability of the enceladus plumes: Orbital periods, decadal periods, and aperiodic change. *Icarus*, *344*. doi: 10.1016/j.icarus.2019.06.006

Ingersoll, A. P., & Nakajima, M. (2016). Controlled boiling on enceladus. 2. model of the liquid-filled cracks. *Icarus*, *272*. doi: 10.1016/j.icarus.2015.12.040

Jaccard, C. (1976). P. v. hobbs ice physics. oxford, clarendon press, 1974. xvii, 837 p. £29. *Journal of Glaciology*, *17*. doi: 10.3189/s0022143000030847

Lau, H. C., Yang, H. Y., Tromp, J., Mitrovica, J. X., Latychev, K., & Al-Attar, D. (2015). A normal mode treatment of semi-diurnal body tides on an aspherical, rotating and anelastic earth. *Geophysical Journal International*, *202*. doi: 10.1093/gji/ggv227

Levinson, M. (1981). A new rectangular beam theory. *Journal of Sound and Vibration*, *74*. doi: 10.1016/0022-460X(81)90493-4

Love, A. E. H. (1909). The yielding of the earth to disturbing forces. *Proceedings of the Royal Society of London. Series A, Containing Papers of a Mathematical and Physical Character*, *82*. doi: 10.1098/rspa.1909.0008

Mancktelow, N. S. (1999). Finite-element modelling of single-layer folding in elasto-viscous materials: The effect of initial perturbation geometry. *Journal of Structural Geology*, *21*. doi: 10.1016/S0191-8141(98)00102-3

McKinnon, W. B. (2015). Effect of enceladus's rapid synchronous spin on interpretation of cassini gravity. *Geophysical Research Letters*, *42*. doi: 10.1002/2015GL063384

McKinnon, W. B., & Melosh, H. J. (1980). Evolution of planetary lithospheres: Evidence from multiringed structures on Ganymede and Callisto. *Icarus*, *44*(2). doi: 10.1016/0019-1035(80)90037-8

Melosh, H. J., & Raefsky, A. (1981). A simple and efficient method for introducing faults into finite element computations. *Bulletin of the Seismological Society of America*, *71*(5). doi: 10.1785/bssa0710051391

Mitri, G., & Showman, A. P. (2005, 10). Convective–conductive transitions and sensitivity of a convecting ice shell to perturbations in heat flux and tidal-heating rate: Implications for Europa. *Icarus*, *177*(2), 447–460. doi: 10.1016/J.ICARUS.2005.03.019

Murray, C. D., & Dermott, S. F. (2000). *Solar System Dynamics*. doi: 10.1017/cbo9781139174817

Neumeier, J. J. (2018). Elastic constants, bulk modulus, and compressibility of h2o ice i h for the temperature range 50 k-273 k. *Journal of Physical and Chemical Reference Data*, *47*. doi: 10.1063/1.5030640

Nimmo, F., Bills, B. G., & Thomas, P. C. (2011). Geophysical implications of the long-wavelength topography of the Saturnian satellites. *Journal of Geophysical Research E: Planets*, *116*(11). doi: 10.1029/2011JE003835

Nimmo, F., & Pappalardo, R. T. (2004). Furrow flexure and ancient heat flux on ganymede. *Geophysical Research Letters*, *31*. doi: 10.1029/2004GL020763

Nimmo, F., Thomas, P. C., Pappalardo, R. T., & Moore, W. B. (2007). The global shape of europa: Constraints on lateral shell thickness variations. *Icarus*, *191*. doi: 10.1016/j.icarus.2007.04.021

Porco, Dinino, D., & Nimmo, F. (2014). How the geysers, tidal stresses, and thermal emission across the south polar terrain of enceladus are related. *Astronomical Journal*, *148*. doi: 10.1088/0004-6256/148/3/45

Porco, Helfenstein, P., Thomas, P. C., Ingersoll, A. P., Wisdom, J., West, R., & Squyres, S. (2006). Cassini observes the active south pole of enceladus. *Science*, *311*. doi: 10.1126/science.1123013

Proctor, T. M. (1966). Low-temperature speed of sound in single-crystal ice. *Journal of the Acoustical Society of America*, *39*. doi: 10.1121/1.1909980

Qin, C., Zhong, S., & Wahr, J. (2014). A perturbation method and its application: Elastic tidal response of a laterally heterogeneous planet. *Geophysical Journal International*, *199*. doi: 10.1093/gji/ggu279

Ramillien, G., Cazenave, A., & Brunau, O. (2004). Global time variations of hydrological signals from grace satellite gravimetry. *Geophysical Journal International*, *158*. doi: 10.1111/j.1365-246X.2004.02328.x

Roberts, J. H., & Nimmo, F. (2008, 4). Tidal heating and the long-term stability of a subsurface ocean on Enceladus. *Icarus*, *194*(2), 675–689. doi: 10.1016/J.ICARUS.2007.11.010

Rovira-Navarro, M., Katz, R. F., Liao, Y., van der Wal, W., & Nimmo, F. (2022). The tides of enceladus' porous core. *Journal of Geophysical Research: Planets*, *127*. doi: 10.1029/2021JE007117

Schenk, P. M. (2008). Cartographic and Topographic Mapping of the Icy Satellites of the Outer Solar System. *International Archives of the Photogrammetry, Remote Sensing and Spatial Information Sciences*, *37*.

Schenk, P. M., Clark, R. N., Howett, C. J. A., Verbiscer, A. J., & Waite, J. H. (2018). *Enceladus and the icy moons of saturn.* doi: 10.2458/azu_uapress_9780816537075

Schubert, G., Anderson, J. D., Travis, B. J., & Palguta, J. (2007). Enceladus: Present internal structure and differentiation by early and long-term radiogenic heating. *Icarus*, *188*(2). doi: 10.1016/j.icarus.2006.12.012

Segall, P. (2010). *Earthquake and volcano deformation.* doi: 10.5860/choice.48-0287

Shaw, G. H. (1985). Elastic properties and equation of state of high pressure ice. *The Journal of Chemical Physics*, *84*. doi: 10.1063/1.449897

Simons, M., & Rosen, P. A. (2015). Interferometric Synthetic Aperture Radar Geodesy. In *Treatise on geophysics: Second edition* (Vol. 3). doi: 10.1016/B978-0-444-53802-4.00061-0

Skroch, M., Owen, S., Staten, M., Quadros, R., Hanks, B., Clark, B., & Stimpson, C. (2019). *CUBIT Geometry and Mesh Generation Toolkit 15.4 User Documentation.*

Sládková, K. P., Souček, O., & Běhounková, M. (2021). Enceladus' tiger stripes as frictional faults: Effect on stress and heat production. *Geophysical Research Letters*, *48*. doi: 10.1029/2021GL094849

Souček, O., Běhounková, M., Čadek, O., Hron, J., Tobie, G., & Choblet, G. (2019). Tidal dissipation in Enceladus' uneven, fractured ice shell. *Icarus*, *328*. doi: 10.1016/j.icarus.2019.02.012

Souček, O., Hron, J., Běhounková, M., & Čadek, O. (2016). Effect of the tiger stripes on the deformation of Saturn's moon Enceladus. *Geophysical Research Letters*, *43*(14). doi: 10.1002/2016GL069415

Spencer, J. R., Pearl, J. C., Segura, M., Flasar, F. M., Mamoutkine, A., Romani, P., & Lopes, R. M. (2006). Cassini encounters enceladus: Background and the discovery of a south polar hot spot. *Science*, *311*. doi: 10.1126/science.1121661

Thomas, P. C., Tajeddine, R., Tiscareno, M. S., Burns, J. A., Joseph, J., Loredo, T. J., & Porco, C. (2016). Enceladus's measured physical libration requires a global subsurface ocean. *Icarus*, *264*. doi: 10.1016/j.icarus.2015.08.037

Tyler, R. H. (2020). Heating of enceladus due to the dissipation of ocean tides. *Icarus*, *348*. doi: 10.1016/j.icarus.2020.113821

Van Hoolst, T., Baland, R. M., & Trinh, A. (2016). The diurnal libration and interior structure of enceladus. *Icarus*, *277*. doi: 10.1016/j.icarus.2016.05.025

Vance, S., Behounkova, M., Bills, B. G., Byrne, P., Cadek, O., Castillo-Rogez, J., ... Wang, S. (2021). Distributed geophysical exploration of enceladus and other ocean worlds. *Bulletin of the AAS*, *53*. doi: 10.3847/25c2cfeb.a07234f4

Wahr, Selvans, Z. A., Mullen, M. E., Barr, A. C., Collins, G. C., Selvans, M. M., & Pappalardo, R. T. (2009). Modeling stresses on satellites due to nonsynchronous rotation and orbital eccentricity using gravitational potential theory. *Icarus*, *200*(1). doi: 10.1016/j.icarus.2008.11.002

Wahr, Zuber, M. T., Smith, D. E., & Lunine, J. I. (2006). Tides on Europa, and the thickness of Europa's icy shell. *Journal of Geophysical Research E: Planets*, *111*(12). doi: 10.1029/2006JE002729

Yin, A., & Pappalardo, R. T. (2015). Gravitational spreading, bookshelf faulting, and tectonic evolution of the South Polar Terrain of Saturn's moon Enceladus. *Icarus*, *260*. doi: 10.1016/j.icarus.2015.07.017

Zhong, S., Qin, C., Geruo, G., & Wahr, J. (2012). Can tidal tomography be used to unravel the long-wavelength structure of the lunar interior? *Geophysical Research Letters*, *39*. doi: 10.1029/2012GL052362

Zolotov, M. Y., & Shock, E. L. (2004). A model for low-temperature biogeochemistry of sulfur, carbon, and iron on Europa. *Journal of Geophysical Research E: Planets*, *109*(6). doi: 10.1029/2003JE002194

Čadek, O., Tobie, G., Van Hoolst, T., Lefèvre, A., Mitri, G., Běhounková, M., & Trinh, A. (2016). Enceladus's internal ocean and ice shell constrained from cassini gravity, shape, and libration data. *Geophysical Research Letters*, *43*. doi: 10.1002/2016GL068634